AIAA JOURNAL
Vol. 46, No. 5, May 2008

Approximate Nonlinear Analysis Method for Debonding of Skin/Stringer Composite Assemblies

Enzo Cosentino*
Airbus UK, Ltd., Bristol, England BS99 7AR, United Kingdom
and
Paul M. Weaver†
University of Bristol, Bristol, England BS8 1TR, United Kingdom

DOI: 10.2514/1.31914

A nonlinear approach is developed and used to predict crack initiation in discretely assembled composite panels made from skin and stringers. Particular emphasis is given to stringer run outs within a stiffened panel for the optimization of novel composite wing configurations. The nonlinear structural behavior is obtained by means of the von Karman formulation for moderately large deflections in plates; three-dimensional assemblies are schematized and the effect of eccentricity is included in the simulation. Solutions are calculated by means of a Rayleigh–Ritz approach based on Galerkin's orthogonal eigenfunctions, and a linear elastic fracture mechanics-based model is used to simulate the crack initiation in the critical regions. Numerical results obtained by means of the present method are validated against tests reported in the literature and compared with advanced nonlinear finite element analysis. Limits of applicability and further potential exploitations are discussed. A validation study showed fairly good correlation with reported experimental data.

Nomenclature

$\boldsymbol{A}$, $\boldsymbol{D}$	=	laminate in-plane and transverse stiffness matrices
$\boldsymbol{A}'$, $\boldsymbol{D}'$	=	laminate in-plane and transverse compliance matrices
$\boldsymbol{A}^*$	=	matrix of in-plane flexibility in partially inverted laminate constitutive equations
a	=	crack length
$\boldsymbol{B}$	=	laminate coupling stiffness matrix
$\boldsymbol{B}'$	=	laminate coupling compliance matrix
$\boldsymbol{B}^*$	=	coupling matrix in partially inverted laminate constitutive equations
$\boldsymbol{D}^*$	=	matrix of reduced flexural stiffness matrices in partially inverted laminate constitutive equations
e	=	neutral-plane function
e_i	=	generalized coordinates of the neutral-plane function
l_x, l_y	=	length and width of panel
$\boldsymbol{N}$, $\boldsymbol{M}$	=	stress, bending moment resultant vectors
N_x, N_y, N_{xy}	=	external in-plane load per unit width
$N_{x,o}$, $N_{y,o}$, $N_{xy,o}$	=	internal in-plane load per unit width
U	=	internal elastic potential energy
u, v	=	in-plane displacement in x and y directions
w	=	out-of-plane displacement
w_i	=	generalized coordinates of the displacement function
X, Y	=	beam eigenfunctions
Φ_i	=	panel eigenfunctions
Ω_N	=	potential of external in-plane loads
Ω_Q	=	potential of external transverse loads

Received 2 May 2007; revision received 5 October 2007; accepted for publication 19 November 2007.

*Composite Stress Analysis, Composite Structures Development Centre; enzo.cosentino@airbus.com.

†Reader, Advanced Composite Centre for Innovation and Science, Department of Aerospace Engineering, Queens Building 2.39, University Walk. Member AIAA.

I. Introduction

THE use of cocured or cobonded structures (Fig. 1) in aerospace potentially offers significant weight reduction over conventional fasteners. Continuous fiber reinforced polymer matrix composites have been gaining wide acceptance as structural materials. Unfortunately, the vulnerability of such structures to through-thickness stresses is well known. This weakness is particularly exacerbated in critical areas such as the skin/stringer overlap in cocured or cobonded stiffened panels or thick sectioned run-out regions, for which the necessity to terminate stiffeners contrasts with the allowable strain requirements.

Skin/stringer interface or run-out tips are vulnerable areas due to geometrical effects and mechanical load paths. Despite their high level of performance in specific areas, such as weight, durability, and through-life costs, composites are often used at relatively low strain levels in primary structures due, in part, to poor through-thickness failure characteristics. This has lead to relatively slow take up within primary flight structures. This delay is mostly due to a reduced understanding of the failure mechanisms and their behavior when damaged. The widespread lack of knowledge and know how often leads to oversized structures, which are in contrast to the lightweight philosophy characterizing new design solutions. In cocured skin/stringer panels, failure often occurs due to delamination and/or debonding at the stiffener foot tip rather than to overall strain limitations. Other critical locations are the core (noodle) and the corner radius, as shown in Fig. 2

Several test programs have shown that the critical load condition that leads the noodle to failure is the out-of-plane load on the stiffener web [1] (Fig. 3a). Nevertheless, tip failure (Figs. 3b and 3c) is the most important failure mode, because it is related to several load conditions.

Several studies [2–5] have shown that the onset of debonding may be caused by the differential stiffness at the interface between the skin and the cocured/cobonded surface. Skin deflection causes the onset of peeling moments and tractions that trigger the first and the second crack opening modes. Furthermore, stress concentration and free edge effect due to material anisotropy can exacerbate the failure

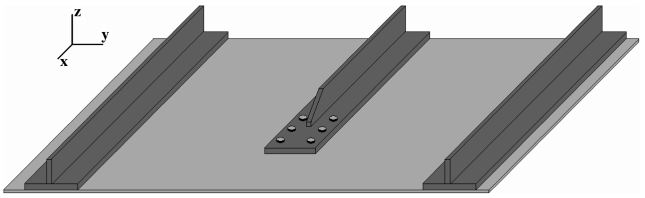

Fig. 1 Example of skin/stringer assemblies.

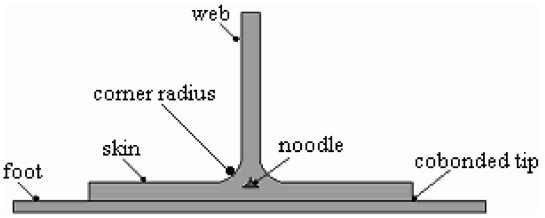

Fig. 2 Main failure initiation areas.

phenomenon by triggering significant through-thickness local effects. For these reasons, the out-of-plane displacement of the skin is one of the foremost concerns for composite designers. The transverse skin displacement is intrinsically present in such structures. The structural role skins perform leads to several load conditions, such as fuel pressure or differential pressure (due to the lift) in wing boxes, internal pressurization in fuselages, and also eccentric in-plane load paths (e.g., stringer run outs). Each of these causes the skin to displace transversely to satisfy static equilibrium. Failure often occurs due to crack initiation at critical locations and subsequent propagation from the initial layer through the entire structure jumping from one layer to the next, in such a manner that leads to catastrophic failure [2,6]. Although the structure may withstand deformations and loads several times larger than the ones corresponding to the first crack (initial failure), the sizing criterion must preserve the total integrity of the structure. This sizing criterion must prevent initial cracking at the most critical locations. The situation is exacerbated because it appears [6,7] that cracks cannot be forced to grow stably within a predetermined path.

Corradi-Dell'Acqua [8] shows that the novel advanced nonlinear finite element (FE) analyses combined with ad hoc failure criteria based on the virtual crack closure technique [9] or ABAQUS [10] standard cohesive elements match test responses fairly well. Unfortunately, the computational effort required to run a reliable and representative virtual test program remain significant. Furthermore, the crack-initiation response of stress-based cohesive elements can be mesh dependant. Therefore, sometimes results have to be interpreted by means of a priori careful considerations and engineering judgment. In light of these considerations, it is clearly evident that there is a need for an alternative method able to provide a quicker solution of the nonlinear problem and to replace the complexity of FE preprocessing. Particularly, in the preliminary stages of structural design, a significant amount of load cases have to be assessed. Hence, a simple but accurate analysis method that only demands a small fraction of the computational efforts required by purely numerical simulations is highly desirable. In this paper, the solution proposed by Timoshenko et al. [11,12] is enhanced to account for anisotropy and solved by means of a nonlinear Rayleigh–Ritz approach using orthogonal eigenfunctions as basis functions. The presence of stiffeners is represented as discontinuous section properties and the function describing the neutral plane of the assembly is treated as an initial (relatively) small perturbation [12]. To avoid potential numerical instabilities due to the discontinuity of the initial displacement function, the problem will be expressed by means of a generalized Galerkin technique, such that highly localized effects are ameliorated. The current work was conducted with the purpose of developing a fast and reliable method of predicting failure loads for stringer run outs. Nevertheless, further applicability of the method is rather broader. The accurate determination of buckling loads for aerospace panels with nonconstant transverse sections or the assessment of out-of-plane displacement of eccentrically in-plane loaded stiffened panels are only a few examples of the potential use of the present analysis.

II. Outline of the Approach

The purpose of the present study is to establish a methodology to predict static initial failure loads of composite skin/stiffeners assemblies. Two linked analytical models are used. The first model has already been briefly described and will now be discussed in depth. It is a nonlinear approach, which provides the stress and displacement fields throughout the domain. The second model is based on a linear elastic fracture mechanics (LEFM) approach first proposed by Williams [3] for one-dimensional beam analyses and enhanced in the present paper to include two-dimensional anisotropic cases. Closed-form equations are developed to calculate the total strain energy release rate (SERR) at the critical interfaces. The total contribution is then partitioned into its elementary contributions (excitations of modes I and II), and a failure criterion is proposed [13] to assess the actual reserve factor.

III. Field Equations

The use of the von Karman nonlinear approach, which is an extension of the Kirchhoff linear model for plates, guarantees that the field equations can be expressed by means of two variables only, that is, the transverse deflection w and the Airy stress function Ψ [14]. To employ a two-dimensional approach, the problem is simplified by locally homogenizing the beam properties of the stiffeners over the plate. This is done by first calculating the axial and bending stiffnesses of the stringer and then locally adding an equivalent layer to the stacking sequence of the skin. The overlapping areas will be assumed to be the projections of the skin/stiffeners contact surfaces on the x–y plane, as described in Fig. 4. The global domain will therefore be partitioned into subdomains (fields). The assumptions made and the procedure that allows the calculation of the equivalent layers and, hence, the properties of each field are described in Appendix A.

The equivalent field properties are then locally smeared over the regions defined by the boundaries of the stiffeners' feet (areas in gray, Fig. 4). Abrupt discontinuities of the functions expressing the neutral plane (loads eccentricity) and the structural properties (i.e., $\boldsymbol{A}$, $\boldsymbol{B}$, and $\boldsymbol{D}$ matrices) occur on the same boundaries.

Following von Karman, the membrane strains and the curvatures are expressed as functions of the transverse displacement as follows:

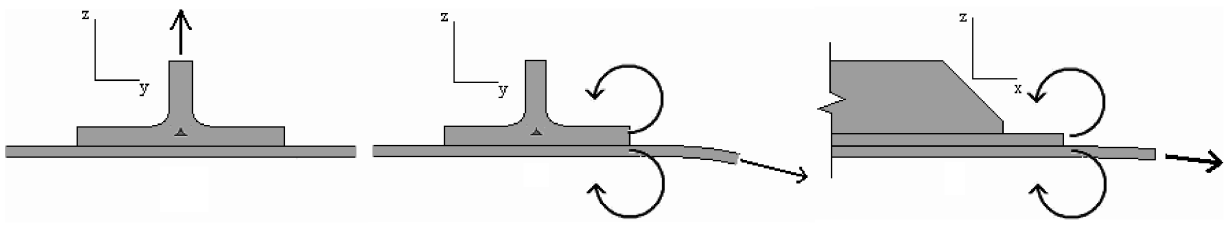

Fig. 3 Typical failure modes: a) noodle failure mode, b) lateral failure mode, and c) tip failure mode.

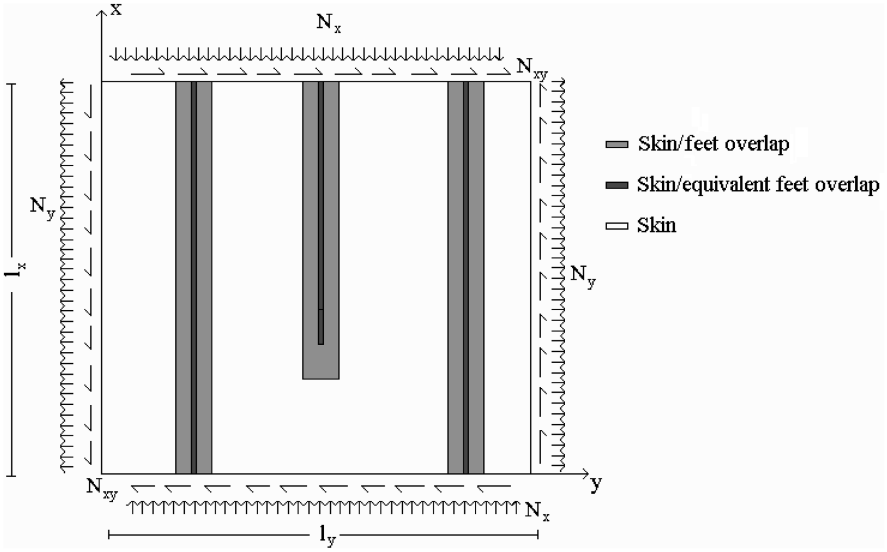

Fig. 4 In-plane projection of the skin/stringer frame assembly.

$$\varepsilon_x^0 = \frac{\partial u_o}{\partial x} + \frac{1}{2}\left(\frac{\partial w}{\partial x}\right)^2, \qquad \varepsilon_{xy}^0 = \frac{\partial u_0}{\partial y} + \frac{\partial v_0}{\partial x} + \frac{\partial w}{\partial x}\frac{\partial w}{\partial y}$$
$$\varepsilon_y^0 = \frac{\partial v_0}{\partial y} + \frac{1}{2}\left(\frac{\partial w}{\partial y}\right)^2 \tag{1}$$

$$k_x = -\frac{\partial^2 w}{\partial x^2}, \qquad k_x = -\frac{\partial^2 w}{\partial y^2}, \qquad k_{xy} = -2\frac{\partial^2 w}{\partial x \partial y} \tag{2}$$

It is assumed that all of the assemblies are sufficiently thin, so that both the aforementioned kinematical assumptions and the state of plane stress required by classical laminate theory are obeyed. According to this assumption, the constitutive equations of the laminate expressed in the partially inverted form are [15,16]

$$\begin{bmatrix} \boldsymbol{\varepsilon}^0 \\ \boldsymbol{M} \end{bmatrix} = \begin{bmatrix} \boldsymbol{A}^* & \boldsymbol{B}^* \\ -\boldsymbol{B}^{*T} & \boldsymbol{D}^* \end{bmatrix} \begin{bmatrix} \boldsymbol{N} \\ \boldsymbol{k} \end{bmatrix} \tag{3}$$

where

$$\boldsymbol{\varepsilon}^0 = \begin{bmatrix} \varepsilon_x^0 \\ \varepsilon_y^0 \\ \varepsilon_{xy}^0 \end{bmatrix}, \qquad \boldsymbol{k} = \begin{bmatrix} k_x \\ k_y \\ k_{xy} \end{bmatrix}$$
$$\boldsymbol{N} = \begin{bmatrix} N_x \\ N_y \\ N_{xy} \end{bmatrix}, \qquad \boldsymbol{M} = \begin{bmatrix} M_x \\ M_y \\ M_{xy} \end{bmatrix} \tag{4}$$

We consider the rectangular panel sketched in Fig. 4 with no predefined boundary conditions. The panel is subjected to uniformly distributed in-plane loads N_x, N_y, and N_{xy} around the edges. Furthermore, the effect of a transverse load $q(x, y)$ is included in the model. Following, for example, Kollar and Springer [17] and Reddy [16], the total strain energy U due to bending is

$$U = \frac{1}{2}\int_0^{l_x}\int_0^{l_y} \boldsymbol{k}^T \boldsymbol{M}\, \mathrm{d}x\mathrm{d}y = \frac{1}{2}\int_0^{l_x}\int_0^{l_y} \boldsymbol{k}^T \boldsymbol{D}^* \boldsymbol{k}\, \mathrm{d}x\mathrm{d}y$$
$$= \frac{1}{2}\int_0^{l_x}\int_0^{l_y}\left[D_{11}^*\left(\frac{\partial^2 w}{\partial x^2}\right)^2 + D_{22}^*\left(\frac{\partial^2 w}{\partial y^2}\right)^2 + 4D_{66}^*\left(\frac{\partial^2 w}{\partial x \partial y}\right)^2\right.$$
$$\left. + 2D_{12}^*\frac{\partial^2 w}{\partial x^2}\frac{\partial^2 w}{\partial y^2} + 4D_{16}^*\frac{\partial^2 w}{\partial x^2}\frac{\partial^2 w}{\partial x \partial y} + 4D_{26}^*\frac{\partial^2 w}{\partial y^2}\frac{\partial^2 w}{\partial x \partial y}\right]\mathrm{d}x\mathrm{d}y \tag{5}$$

If the in-plane loads do not vary with x and y, the in-plane equation involving the Airy stress function is identically satisfied, and the potential Ω_N of external in-plane forces is [11,17]

$$\Omega_N = \frac{1}{2}\int_0^{l_x}\int_0^{l_y}\left[N_{x,0}\left(\frac{\partial w}{\partial x} + \frac{\partial e}{\partial x}\right)^2 + N_{y,0}\left(\frac{\partial w}{\partial y} + \frac{\partial e}{\partial y}\right)^2\right.$$
$$\left. + 2N_{xy,0}\frac{\partial (w+e)}{\partial x}\frac{\partial (w+e)}{\partial y}\right]\mathrm{d}x\mathrm{d}y \tag{6}$$

where $e(x, y)$ is the neutral-plane function that is treated as a moderately large initial perturbation, and $N_{x,o}$, $N_{y,o}$, and $N_{xy,o}$ are the internal in-plane forces per unit length that are related to the external applied loads as shown in Appendix B. Similarly, the potential Ω_Q of the transverse load is [17]

$$\Omega_Q = -\int_0^{l_x}\int_0^{l_y} q w\, \mathrm{d}x\mathrm{d}y \tag{7}$$

The total potential energy Π of the system is therefore

$$\Pi = U + \Omega_N + \Omega_Q \tag{8}$$

To use the Rayleigh–Ritz method, an approximate expression for the unknown variable w in generalized coordinates is required, which identically satisfies the geometric boundary conditions. The following series expansion satisfies the aforementioned conditions:

$$w = \sum_{m=1}^{M}\sum_{n=1}^{N} w_{mn} X_m(x) Y_n(y) \tag{9}$$

where $X_m(x)$ and $Y_n(y)$ are continuous and indefinitely differentiable functions. Wherever possible, the use of beam eigenfunctions that satisfy the following orthogonality relations is recommended:

$$\int_0^{l_x} X_p(x) X_q(x)\, \mathrm{d}x: \begin{cases} =0 & p \neq q \\ \neq 0 & p = q \end{cases}$$
$$\int_0^{l_y} Y_p(x) Y_q(x)\, \mathrm{d}x: \begin{cases} =0 & p \neq q \\ \neq 0 & p = q \end{cases} \tag{10}$$

To simplify the syntax of the expressions and be able to use one index only, the following vectors are defined:

$$\boldsymbol{\Phi} = [X_1 Y_1\, X_1 Y_2 \cdots X_1 Y_N\, X_2 Y_1 X_1 Y_2 \cdots X_2 Y_N \cdots X_M Y_1\, X_M Y_2\, X_M Y_N]^T$$
$$\mathbf{W} = [w_1\, w_2 \cdots w_{M\times N}]^T \tag{11}$$

Equation (9) can therefore be rewritten, more simply, as

$$w = \sum_{i=1}^{M\times N} w_i \phi_i(x, y) \tag{12}$$

where it is straightforward to show that, if conditions in Eq. (10) apply, the functions Φ_i satisfy the following two-dimensional orthogonality relations:

$$\int_0^{l_x}\int_0^{l_y} \phi_i(x, y)\phi_j(x)\,\mathrm{d}x\mathrm{d}y: \begin{cases} =0 & i \neq j \\ \neq 0 & i = j \end{cases} \tag{13}$$

Equation (12) combined with the definition of functions $X_m(x)$ and $Y_n(y)$ guarantees that every function defined inside the considered domain and fulfilling the same essential boundary conditions as the panel can be expressed as a linear combination of such eigenfunctions. If M and N are reasonably large integers, then the error committed when truncating the summation is negligible. Yet, generic functions defined with different boundary conditions inside the domain can be expressed as truncated linear combinations by means of a Galerkin technique [18]. The initial perturbation $e(x, y)$ can therefore be expressed as follows (see Appendix C for details):

$$e = \sum_{i=1}^{M\times N} e_i \phi_i(x, y) \tag{14}$$

Expressing the neutral plane as a linear combination of the same base functions will allow differentiating the total potential energy in a closed form, obtaining a final compact form, which is derived and expressed in Eq. (19) and also easily implemented in software.

Substituting Eqs. (12) and (14) into Eqs. (5–7) the total potential is expressed as a second order polynomial of the $M \times N$ unknown coefficients w_i. Expressions for U, Ω_N, and Ω_Q are reported as follows:

$$\begin{aligned} U = \frac{1}{2}\int_0^{l_x}\int_0^{l_y} \sum_{i=1}^{M\times N}\sum_{j=1}^{M\times N} (&D_{11}^*\phi_{,xx,i}\,\phi_{,xx,j} + D_{22}^*\phi_{,yy,i}\,\phi_{,yy,j} \\ &+ 4D_{66}^*\phi_{,xy,i}\,\phi_{,xy,j} + 2D_{12}^*\phi_{,xx,i}\,\phi_{,yy,j} + 4D_{16}^*\phi_{,xx,i}\,\phi_{,xy,j} \\ &+ 4D_{26}^*\phi_{,yy,i}\,\phi_{,xy,j})w_i w_j\,\mathrm{d}x\mathrm{d}y \end{aligned} \tag{15}$$

$$\begin{aligned} \Omega_N = \frac{1}{2}\int_0^{l_x}\int_0^{l_y} \sum_{i=1}^{M\times N}\sum_{j=1}^{M\times N} (&N_{x,o}\phi_{,x,i}\,\phi_{,x,j} + N_{y,o}\phi_{,y,i}\,\phi_{,y,j} \\ &+ 2N_{xy,o}\phi_{,x,i}\,\phi_{,y,j})(w_i + e_i)(w_j + e_j)\,\mathrm{d}x\mathrm{d}y \end{aligned} \tag{16}$$

$$\Omega_Q = -\int_0^{l_x}\int_0^{l_y} q(x, y)\sum_{i=1}^{M\times N}\phi_i w_i\,\mathrm{d}x\mathrm{d}y \tag{17}$$

The principle of stationary potential energy states that

$$\frac{\partial\Pi}{\partial w_i} = 0, \quad \forall\ i = 1, \ldots, M \times N \tag{18}$$

Equations (15–17) are now substituted into Eq. (18) with the result differentiated with respect to w_i. Algebraic manipulations result in the following linear system of $M \times N$ equations in the $M \times N$ unknowns w_i, $i = 1, \ldots, N$:

$$(\boldsymbol{G} + \boldsymbol{H})\boldsymbol{W} = -\boldsymbol{H}\boldsymbol{E} + \boldsymbol{Q} \tag{19}$$

where the vectors $\boldsymbol{Q}$ and $\boldsymbol{E}$ and the matrices $\boldsymbol{G}$ and $\boldsymbol{H}$ are defined as

$$\boldsymbol{Q}_i = \int_0^{l_x}\int_0^{l_y} q\phi_i\,\mathrm{d}x\mathrm{d}y \tag{20}$$

$$\boldsymbol{E} = [e_1 \quad e_2 \cdots e_{M\times N}]^T \tag{21}$$

$$\begin{aligned} [\boldsymbol{G}]_{ij} = \frac{1}{2}\int_0^{l_x}\int_0^{l_y} &[2D_{11}^*\phi_{,xx,i}\,\phi_{,xx,j} + 2D_{22}^*\phi_{,yy,i}\,\phi_{,yy,j} \\ &+ 8D_{66}^*\phi_{,xy,i}\,\phi_{,xy,j} + 2D_{12}^*(\phi_{,xx,i}\,\phi_{,yy,j} + \phi_{,xx,j}\,\phi_{,yy,i}) \\ &+ 4D_{16}^*(\phi_{,xx,i}\,\phi_{,xy,j} + \phi_{,xx,j}\,\phi_{,xy,i}) \\ &+ 4D_{26}^*(\phi_{,yy,i}\,\phi_{,xy,j} + \phi_{,yy,j}\,\phi_{,xy,i})]\,\mathrm{d}x\mathrm{d}y \end{aligned} \tag{22}$$

$$\begin{aligned} [\boldsymbol{H}]_{ij} = \frac{1}{2}\int_0^{l_x}\int_0^{l_y} &[2N_{x,o}\phi_{,x,i}\,\phi_{,x,j} + 2N_{y,o}\phi_{,y,i}\,\phi_{,y,j} \\ &+ 2N_{xy,o}(\phi_{,x,i}\,\phi_{,y,j} + \phi_{,x,j}\,\phi_{,y,i})]\,\mathrm{d}x\mathrm{d}y \end{aligned} \tag{23}$$

The system described by Eq. (19) is invertible and yields the $M \times N$ coefficients w_i, which will completely describe the state of stress and strain throughout the domain.

IV. Debond Model

Two main approaches to model crack failure have emerged during the last few decades: the *strength of material*-based approach, which remains by far the most commonly accepted in the industry, and the *fracture mechanics*-based approach. Argawal [19] and Hachenberg and Kossira [7] applied the strength of material approach, which was the most prevalent approach until relatively recently. Developments in fracture mechanics of fiber reinforced composite materials offer the advantage of implementing closed-form expressions to describe the material behavior. Nevertheless, simple expressions such as power laws [1,13] allow easy calibration by *tuning* the exponents to fit test responses. The approach chosen in the present paper to simulate debonding was first developed by Williams [3] for isotropic one-dimensional configurations and enhanced here to account for two-dimensional orthotropic problems. The method follows two steps. In the first step, strain energy release rates ($G_{\mathrm{tot,I}}$ and $G_{\mathrm{tot,II}}$) are calculated as functions of the local values of normal in-plane stress resultants and transverse bending resultants. In the second step, a power law [13] is used to predict crack initiation due to the interaction of modes I and II (mixed mode). Our motivation to follow the approach as outlined comes partly from the work of Taki and Kitagawa [1], who used a simplified version of the present model to predict skin/stiffener debonding in the postbuckling regime of composite stiffened panels and whose predictions matched experimental results fairly well. To account for biaxial loading, an enhanced version of the approach is proposed in the present study. In the following discussion, the contribution of the vertical shear is neglected but mode II contributions from in-plane loads and bending [3] are included in the model. Furthermore, mode III contributions to the total SERR are omitted, such that the initial failure is attributed to the first and second (the peeling mode I and the sliding mode II) opening modes.

The most critical zones for the configuration represented in Fig. 5 are usually the ones in which geometrical discontinuities are present. These discontinuities can lead to local stress concentrations, causing interlaminar crack growths that may originate either inside the bonded interface (adhesive/cohesive failure) or inside the material itself (material failure/delamination) and then propagate through the composite layers.

Several test programs [2,6,20] with the aim of understanding failure mechanisms in stringer run-out tips have shown that statistically the crack starts inside the interface layer and then propagates though the laminate, jumping from layer to layer before leading to catastrophic failure. Further studies have been conducted to decompose the total contribution into the components of modes I and II [5]. The location of crack initiation and the final cause of failure is important because it allows the appropriate choice of material properties to fully characterize the phenomenon. In general, failure occurs due to the mixed mode, in an unknown proportion,

which depends upon the applied load and the mechanical and geometrical parameters. Locally, the presence of a discontinuity and therefore of a differential stiffness generates stress concentrations, which, combined with a possible edge effect, causes interlaminar shears and tensile out-of-plane normal tensions exciting, respectively, the peeling mode I and the sliding mode II.

Laminates containing flaws respond in an approximately linear elastic manner [3], hence, a linear elastic approach can be used to calculate the strain energy release rate. Referring to Fig. 5, it is well known that the total strain energy release rate G_{tot} may be defined as follows:

$$G_{\text{tot}} = \frac{1}{L}\left(\frac{\mathrm{d}U_e}{\mathrm{d}a} - \frac{\mathrm{d}U_s}{\mathrm{d}a}\right) \tag{24}$$

where L is the width of the cracked region, a is the crack length, $\frac{\mathrm{d}U_e}{\mathrm{d}a}$ is the external work performed for the contour defining the crack surface, and $\frac{\mathrm{d}U_s}{\mathrm{d}a}$ is the internal strain energy increment for the contour defining the crack surface.

It can be shown [4] that expressions for total SERRs G^M_{tot} and G^N_{tot}, respectively, due to bending and in-plane tension are

$$G^M_{\text{tot}} = \tfrac{1}{2}\left[D'_{11,\text{top}}M^2_{x,\text{top}} + D'_{11,\text{bot}}M^2_{x,\text{bot}} - D'_{11}M^2_x\right] \tag{25}$$

$$G^N_{\text{tot}} = \tfrac{1}{2}\left[A'_{11,\text{top}}N^2_{x,\text{top}} + A'_{11,\text{bot}}N^2_{x,\text{bot}} - A'_{11}N^2_x\right] \tag{26}$$

where G^M_{tot} is the total SERR due to the transverse bending moment, G^N_{tot} is the total SERR due to the in-plane load, N_x is $N_{x,\text{top}} + N_{x,\text{bot}}$, and M_x is $M_{x,\text{top}} + M_{x,\text{bot}}$.

These expressions represent both the differential stiffness and load transfer, because the latter is not defined a priori, such that the lower load is calculated whereas the upper load is assumed to be zero. If a unit width is considered, then M_x, $M_{x,\text{top}}$, and $M_{x,\text{bot}}$ are the bending moments per unit width and, similarly, N_x, $N_{x,\text{top}}$, and $N_{x,\text{bot}}$ are the in-plane stress resultants per unit width. Note that Eqs. (25) and (26) remain valid if a discontinuity and therefore a crack propagation in the y direction is considered, under the caveat of exchanging the x subscript with y and A'_{11} and D'_{11} with A'_{22} and D'_{22}, respectively. The total SERR is obtained by summing both the in-plane and the transverse contributions as follows:

$$G_{\text{tot}} = G^N_{\text{tot}} + G^M_{\text{tot}} \tag{27}$$

Equations (25) and (26) enable G^M_{tot} and G^N_{tot} to be calculated from the local values of stress resultants at the crack tip. No energy or local three-dimensional stress field calculations are required. Therefore, the classical two-dimensional theory of plates is satisfactory for a full representation of the problem. It must be emphasized that tapered terminations (e.g., ply drop offs) cannot be modeled by means of the present analysis. An abrupt discontinuity at the crack tip is required to employ Eqs. (25) and (26).

The criterion proposed to estimate the onset of fracture is a power law first used by Wu [13] and reported hereafter in the general form:

$$\left(\frac{G_{\text{tot,I}}}{G_{\text{I},C}}\right)^{\xi} + \left(\frac{G_{\text{tot,II}}}{G_{\text{II},C}}\right)^{\eta} = 1 \tag{28}$$

where $G_{\text{tot,I}}$ is the total strain energy release rate for mode I, $G_{\text{tot,II}}$ is the total strain energy release rate for mode II, $G_{\text{I},C}$ is the critical strain energy release rate for mode I, $G_{\text{II},C}$ is the critical strain energy release rate for mode II, and ξ and η are constants.

The general form of the proposed interaction law allows *tuning* the values of exponents ξ and η. This feature enhances the efficacy of the model, which can be calibrated (e.g., for industrial applications) to match available experimental data. The values $\xi = 2$ and $\eta = 2$ are chosen in the present study because they provide good correlation with the experimental and numerical cases examined.

To apply Eq. (28), the total contributions of in-plane and transverse bending resultants must be partitioned into pure peeling and pure sliding components. Following Williams [3], and assuming that for finite discontinuities at critical interfaces, such as those characterizing most of the skin/stringer assemblies, the contributions from uppermost sublaminate above the cracked zone are zero [1],

$$\begin{aligned} G^M_{\text{I}} &= \frac{M^2_x}{2(1+\Psi)^2}[D'_{11,\text{top}} + D'_{11,\text{bot}}] \\ G^M_{\text{II}} &= \frac{M^2_x}{2(1+\Psi)^2}[\Psi^2 D'_{11,\text{bot}} - (1+\Psi)^2 D'_{11}] \end{aligned} \tag{29}$$

$$G^N_{\text{I}} = 0, \qquad G^N_{\text{II}} = G^N_{\text{tot}} = \tfrac{1}{2}N^2_x[A'_{11,\text{bot}} - A'_{11}] \tag{30}$$

where G^M_{I} is the total strain energy release rate for mode I due to bending, G^M_{II} is the total strain energy release rate for mode II due to bending, G^F_{I} is the total strain energy release rate for mode I due to the in-plane load, G^F_{II} is the total strain energy release rate for mode II due to the in-plane load, and Ψ is $D'_{11,\text{top}}/D'_{11,\text{bot}}$.

Assume that the total strain energy release rates for modes I and II are expressed as follows:

$$G_{\text{tot,I}} = G^M_{\text{I}} + G^F_{\text{I}}, \qquad G_{\text{tot,II}} = G^M_{\text{II}} + G^F_{\text{II}} \tag{31}$$

Equations (28–31) combine and lead to the following expression that governs the crack initiation:

$$\left[\frac{M^2_x(D'_{11,\text{top}} + D'_{11,\text{bot}})}{2(1+\Psi)^2 G_{\text{I},C}}\right]^{\xi} + \left[\frac{M^2_x(\Psi^2 D'_{11,\text{bot}} - (1+\Psi)^2 D'_{11})}{2(1+\Psi)^2 G_{\text{II},C}} + \frac{1}{2G_{\text{II},C}}N^2_x(A'_{11,\text{bot}} - A'_{11})\right]^{\eta} = 1 \tag{32}$$

Expressing the moment by means of Eqs. (2), (3), and (12), and calculating the coefficients w_i by inverting Eq. (19), one is able to predict whether failure occurred. If the left-hand side of Eq. (32) is less than unity, then the structure remains undamaged, otherwise a crack has occurred in the analyzed critical location. It must be noted [5] that the component G^M_{I} that depends on bending in the first mode must be considered if a negative curvature k_x is locally present. If such curvature is positive, then G^M_{I} should be set equal to zero [5]. Furthermore, it is worth noting that if a discontinuity along the y direction is analyzed, then Eq. (32) applies if the subscripts x and y are interchanged.

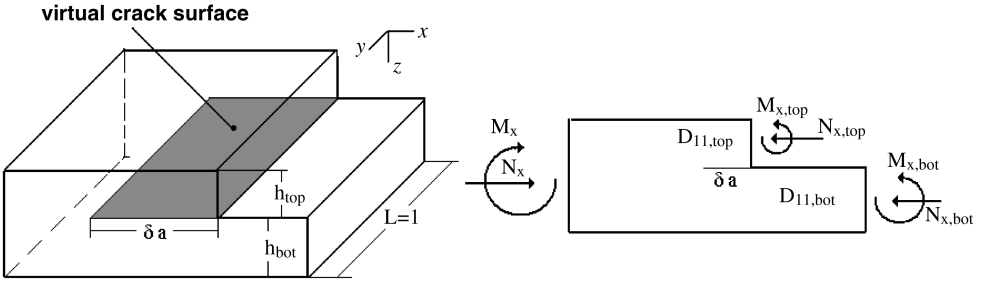

Fig. 5 Crack geometry and schematization.

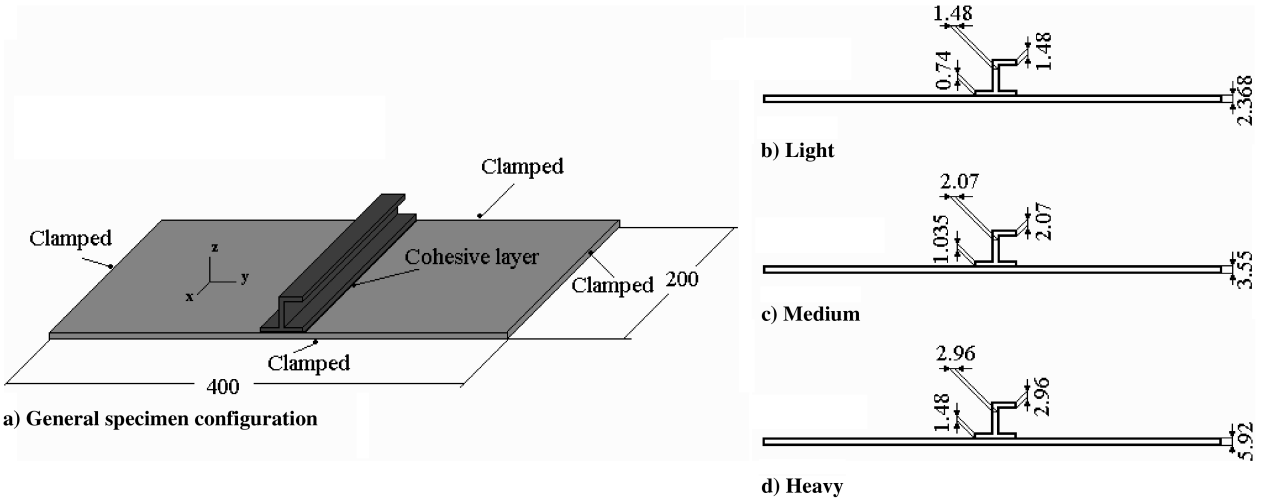

Fig. 6 Virtual specimens, mm.

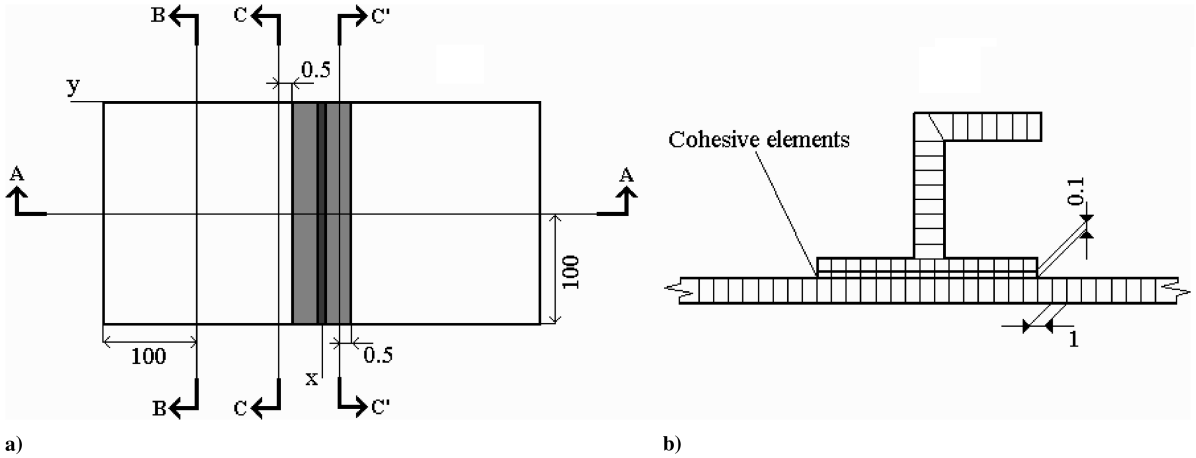

Fig. 7 Plate geometry: a) sections of interest, and b) typical mesh size at the bond line. Dimensions in mm.

V. Model Validation

To validate the accuracy of the present model, three configurations were initially analyzed and the results were compared with nonlinear FE analyses using ABAQUS [10]. Virtual specimens are sketched in Fig. 6.

Continuum shell elements (CH8R) were used to model each lamina and a layer made of cohesive elements (COH3D8) was placed between the upper surface of the skin and the lower surface of the foot to simulate the bond line.

The thickness of the cohesive layer was set to 0.1 mm. Details of mesh size are provided in Fig. 7b. Values of bending moment used in Eq. (32) are taken from the centroids of the elements (output as section moment) and are situated 0.5 mm from the stiffener edge (bond line) according to section C–C in Fig. 7a. The mechanical properties used for each lamina [1] are listed in Table 1.

Details of stacking sequences used to simulate the light, medium, and heavy configurations, respectively, are given in Table 2. The specimens were assumed to be clamped on all the four edges and loaded with a uniformly distributed load in the transverse z direction.

The adopted shape functions are the solutions of Euler's column buckling for a clamped/clamped beam [21]:

$$X_m(x) = a_{1,m} + b_{1,m}x + c_{1,m}\sin\alpha_{1,m}x + d_{1,m}\cos\alpha_{1,m}x \tag{33}$$

$$Y_n(y) = a_{2,n} + b_{2,n}y + c_{2,n}\sin\alpha_{2,n}y + d_{2,n}\cos\alpha_{2,n}y \tag{34}$$

where

Table 1 Material properties for Toho Q-C133 lamina

Material name	Toho Q-C133 (IM600/133)
Longitudinal Young's modulus, E_L, GPa	162
Transverse Young's modulus, E_T, GPa	8.8
In-plane shear modulus, G_{LT}, GPa	4.5
Major Poisson's ratio, ν_{LT}	0.35
Nominal ply thickness, t, mm	0.148
Critical SERR for mode I, G_{IC}, N/mm	0.294
Critical SERR for mode II, G_{IIC}, N/mm	1.370

Table 2 Stacking sequences for the light, medium, and heavy specimen configurations

Coupon type	Light	Medium	Heavy
Skin	$[0/90/45/-45]_S$	$[0/90/45/-45]_{3S}$	$[0/90/45/-45]_{SS}$
Web	$[90/45/-45/0/0/0/0/-45/45/90]$	$[90/45/-45/0/0/45/0/0/45/0/0/-45/45/90]$	$[90/45/-45/0/0/0/0/-45/45/90]_S$
Upper flange	$[90/45/-45/0/0/0/0/-45/45/90]$	$[90/45/-45/0/0/45/0/0/45/0/0/-45/45/90]$	$[90/45/-45/0/0/0/0/-45/45/90]_S$
Foot	$[90/45/-45/0/0]$	$[90/45/-45/0/0/45/0]$	$[90/45/-45/0/0/0/0/-45/45/90]$

Table 3 Roots of associated transcendental Eq. (37)

$m(n)$	1	2	3	4	5	6	7	8	9	10	>10
$\lambda_m(\lambda_n)$	2π	2.863π	4π	4.918π	6π	6.941π	8π	8.955π	10π	10.965π	$(m+1)\pi$

Table 4 Compared failure load predictions for nonsymmetric specimens

	Predicted load level at initial failure, MPa	
	FEM	Closed form
Coupon type		
Light	0.179	0.162
Medium	0.096	0.075
Heavy	0.304	0.332

$$a_{1,m} = -1, \qquad b_{1,m} = -\frac{\alpha_{1,m} l_x (\cos \alpha_{1,m} l_x - 1)}{\alpha_{1,m} l_x - \sin \alpha_{1,m} l_x}$$
$$c_{1,m} = \frac{(\cos \alpha_{1,m} l_x - 1)}{\alpha_{1,m} l_x - \sin \alpha_{1,m} l_x}, \qquad d_{1,m} = 1 \tag{35}$$

$$a_{2,n} = -1, \qquad b_{2,n} = -\frac{\alpha_{2,n} l_y (\cos \alpha_{2,n} l_y - 1)}{\alpha_{2,n} l_y - \sin \alpha_{2,n} l_y}$$
$$c_{2,n} = \frac{(\cos \alpha_{2,n} l_y - 1)}{\alpha_{2,n} l_y - \sin \alpha_{2,n} l_y}, \qquad d_{2,n} = 1 \tag{36}$$

The quantities $\alpha_{1,m}$, $\alpha_{2,n}$ are the roots of the following transcendental equation and are provided in Table 3:

$$\frac{\cos \lambda - 1}{\sin \lambda} - \lambda + \sin \lambda + \frac{\cos \lambda - 1}{\sin \lambda} \cos \lambda = 0, \qquad \lambda = \alpha l \tag{37}$$

where l is the span length of the beam and must be set equal to l_x and l_y (the length and width of the panel) when calculating X_m and Y_n, respectively.

Failure loads at the initiation level calculated by means of the present analysis are compared with the FE analysis predictions in Table 4. The following values were chosen for the exponents of Eq. (32):

$$\xi = 2, \qquad \eta = 2 \tag{38}$$

Furthermore, the global accuracy of the method was validated by comparing the simulation with the FE responses, in terms of out-of-plane deflections and interface peeling moments. Figure 7a shows the locations used for comparison purposes.

The out-of-plane displacements along section lines AA and BB are compared for Light, Medium, and Heavy configurations in Figs. 8–10 respectively, for a transverse load equal to 0.01 MPa.

It is observed that the predicted x-wise out-of-plane displacements fit fairly well with the FE responses. The chordwise (y) displacement comparisons show that the model is slightly stiffer than the FE analysis. This is more evident in the central region in which the stringer lays over the skin.

The local mismatch might be due to the technique used to condense the stringer's properties over the skin. More complicated techniques could be proposed to simulate the presence of the part of the stringer that is not directly in contact with the skin, but this is beyond the purpose of the present study. However, the excess of stiffness causes the predicted peeling moments in the overlap side of the cocured interface (see Fig. 3b) to be slightly overestimated by the analytical model. As a consequence, results tend to be conservative, as shown in Figs. 11–13, in which peeling moments are compared at the skin side (Fig. 7, section CC) and at the overlap side (Fig. 7, section C′C′).

The nonlinearity and the anisotropy of the stacking sequences can induce in-plane membrane loads, which combined with the local eccentricity cause a discontinuity of the bending moments at the skin/foot interface, with an abrupt increment that equals the in-plane membrane load N_y multiplied by the eccentricity (Fig. 14). This effect cannot be properly captured by the analytical model, which is based on eigenfunctions, which are continuous and indefinitely differentiable. There are no discontinuities of curvatures locally; hence, the only abrupt variation of peeling moment is due to the discontinuity of section properties (matrices $\boldsymbol{A}$, $\boldsymbol{B}$, and $\boldsymbol{D}$). However, to properly exploit the LEFM model, the peeling moment that should

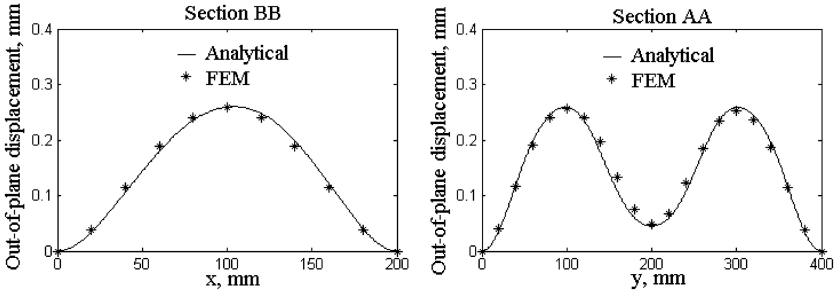

Fig. 8 Out-of-plane displacements for the light configuration.

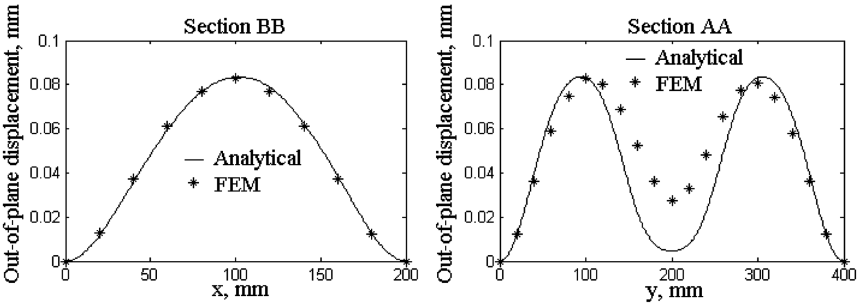

Fig. 9 Out-of-plane displacements for the medium configuration.

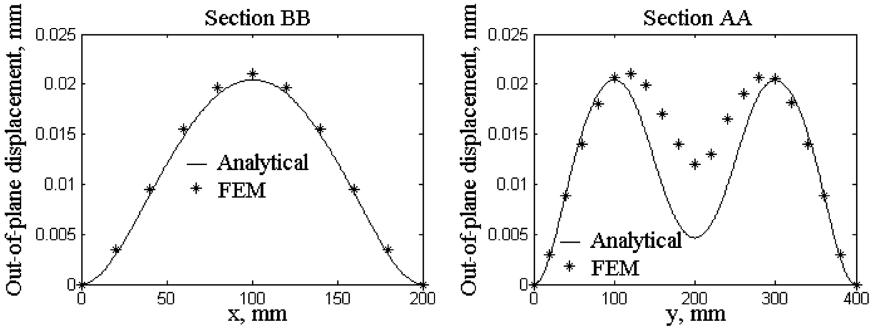

Fig. 10 Out-of-plane displacements for the heavy configuration.

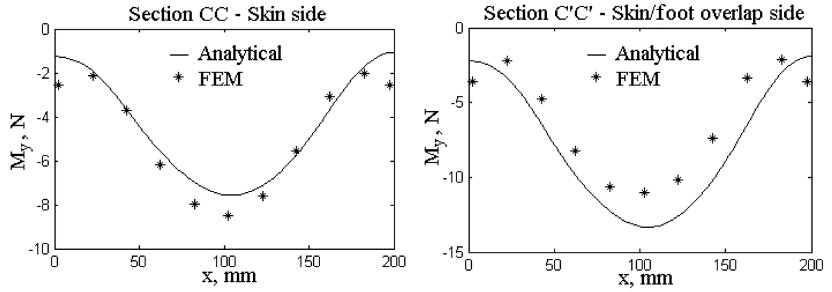

Fig. 11 Compared interface peeling moments M_y for the light configuration.

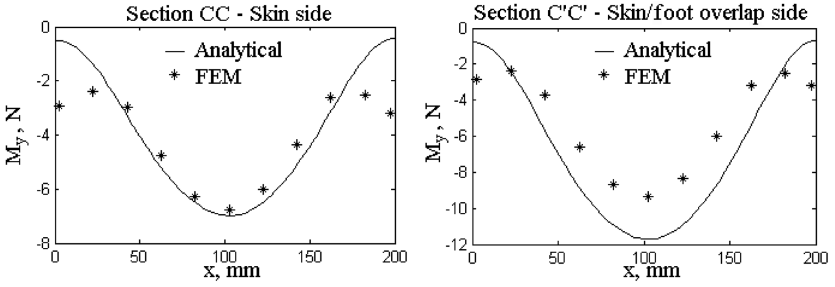

Fig. 12 Compared interface peeling moments M_y for the medium configuration.

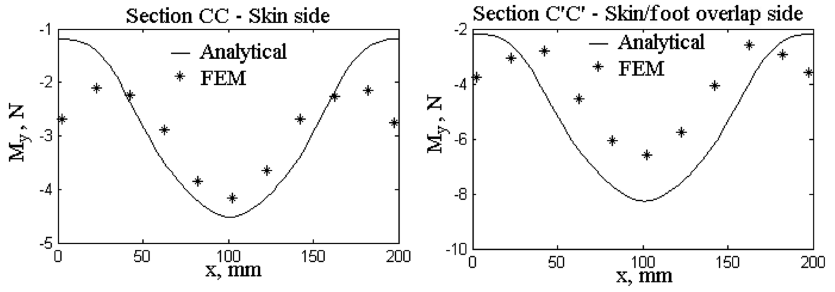

Fig. 13 Compared interface peeling moments M_y for the heavy configuration.

be used to feed Eq. (32) is the overlap side moment because it is capable of performing work when a virtual crack initiates and grows [3].

As visible in Figs. 11–13, the FE analysis predicts local maximum values of bending moments close to the clamped boundaries ($x = 0$, $x = l_x$). This discrepancy is attributed to the induced torsion on the stringer and is not captured by the current method. Figure 15 shows the induced torsion due to the eccentricity d of the shear center. The uneven behavior can appreciably affect the stress field in highly nonlinear regimes. However, for all the examined cases, the maximum moment is registered in the middle of the bay, and both the FE and the analytical analyses predict the initial failure to occur at a span coordinate x approximately equal to $l_x/2$ in the region in which the method fits fairly well with the FE responses. Therefore, the results are believed to be reliable and representative of the real failure mechanism.

Figure 16 shows a second type of stiffened plate, with a symmetric stringer, which was modeled and virtually tested. Three configurations were again virtually tested with ABAQUS and the results were compared with the analytical predictions. Global geometry, material, stacking sequences, and thicknesses are the same as the ones reported in Tables 1 and 2. The only difference is the symmetry of the upper flange. This dissimilarity cannot be captured by the method used to condense the stringer properties over the skin; therefore, analytical calculations do not change.

Peeling moments in the proximity of the bond line (sections are sketched in Fig. 7a) are compared in Figs. 17–19. The FE and analytical predictions agree much better than for the asymmetric

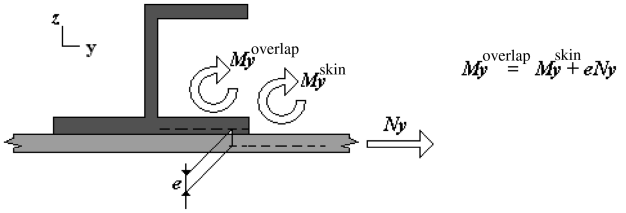

Fig. 14 Cocured (cobonded) interface equilibrium.

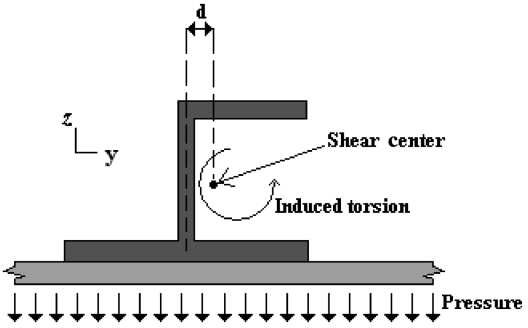

Fig. 15 Induced torsion on the stringer.

upper flange considered previously. As such, the induced torsion does appear to be the cause of the discrepancy of results predicted for the asymmetric flange.

Failure predictions reported in Table 4 show good correlation between the FE analysis and the closed-form solutions. The computational efforts associated with the analytical approach are almost negligible. For a relatively large number of terms used to approximate the displacement ($M = 5, N = 8$), the total calculation time was less that 400 s. If the analysis is applied to calculate deformed shapes only (i.e., to derive out-of-plane displacements in upper and lower wing covers for aerodynamics constraint studies), the number of terms that guarantee convergence is significantly lower and solutions are obtainable in much lower CPU times. This study partly validates the approach and shows that it is suitable for the stage of preliminary structural design, for which a significant amount of load cases have to be assessed and computational efficiency is key. A further study is now undertaken to examine the effect of boundary conditions. Simply supported edges are considered in Fig. 20 and FE simulations are once again compared with analytical predictions.

The adopted shape functions are the solutions of Euler's column buckling for a simply supported beam [21]:

$$X_m(x) = \sin m\pi \frac{x}{l_x}, \qquad Y_n(y) = \sin n\pi \frac{y}{l_y} \tag{39}$$

The out-of-plane displacements were compared and results are reported in Figs. 21–23. Again, Fig. 7a shows the location used for comparison purposes.

The predicted x-wise out-of-plane displacements match the FE responses quite closely. The chordwise (y) displacement comparisons show that the model is able to effectively capture the effect of the stiffener, particularly in the central region in which the stringer lays over the skin.

The model was further validated against the tests done by Falzon and Davies [6]. A total of eight stringer run-out specimens were manufactured and compressively loaded up to the initial failure (debond) of the run-out termination (see Fig. 3c). Two different termination schemes, tapered and nontapered foot, were used. Because the debond model does not allow for tapered terminations, four tests only [6] were compared with the analytical predictions. The tested specimens are schematically described in Figs. 24 and 25. The locations of the strain gauges used for comparison purposes are depicted in Fig. 26. Further details are described in Falzon and Davies [6]. The specimens were not constrained along the edges parallel to the stringer direction (x). The remaining two edges were potted and therefore may be considered clamped for the purpose of this validation. The adopted shape functions are

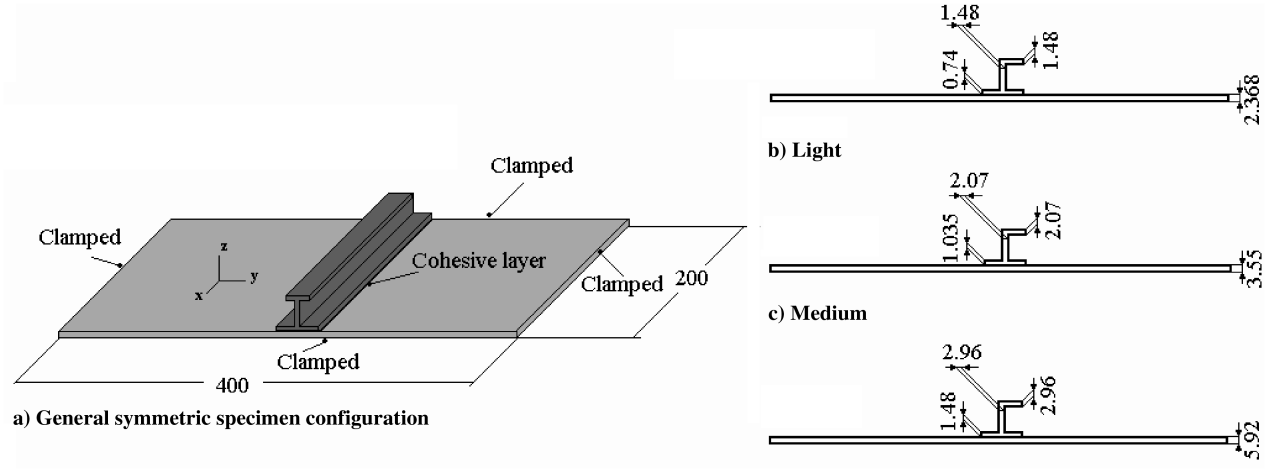

Fig. 16 Symmetrical virtual specimens, mm.

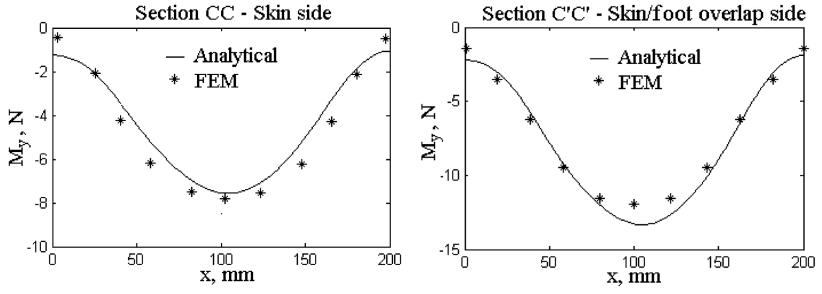

Fig. 17 Compared interface peeling moments M_y for the symmetric light configuration.

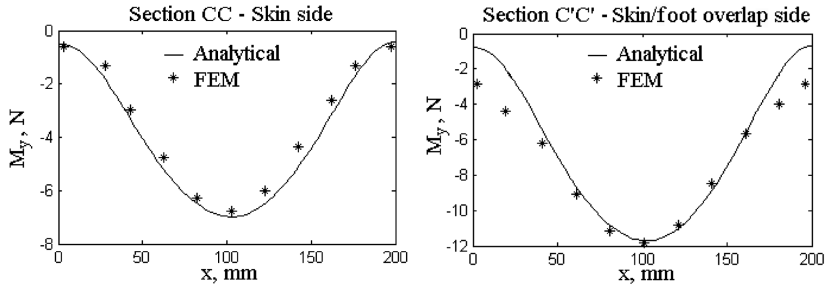

Fig. 18 Compared interface peeling moments M_y for the symmetric medium configuration.

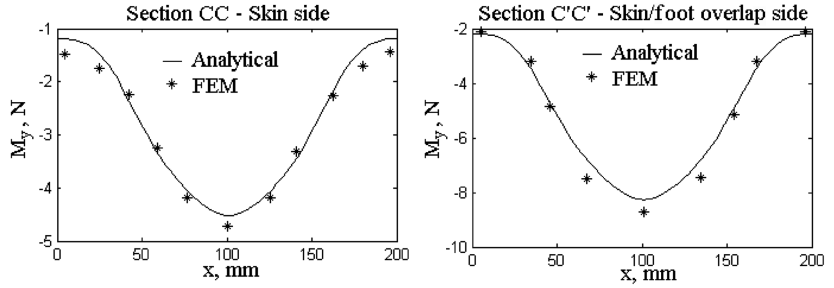

Fig. 19 Compared interface peeling moments M_y for the symmetric heavy configuration.

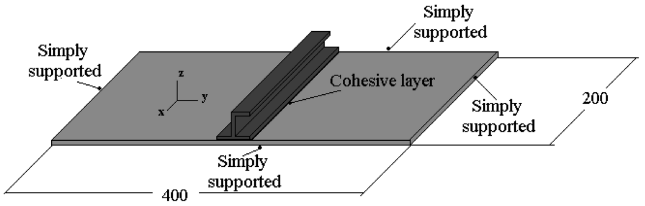

Fig. 20 Simply supported specimen geometry, mm.

$$X_m(x) = a_m + b_m x + c_m \sin \alpha_m x + d_m \cos \alpha_m x \tag{40}$$

and are those already used in the previous section as an x-wise shape function (see Fig. 27 for coordinates datum system). The symmetric solution proposed by Levy for a free–free beam was used as a y-wise shape function [8]:

$$Y_n(y) = \frac{n\pi}{l_x} y \sinh\left(\frac{n\pi y}{l_x}\right) - \left[2 + \frac{n\pi l_y}{2l_x} \tanh\left(\frac{n\pi l_y}{2l_x}\right)\right] \cosh\left(\frac{n\pi y}{l_x}\right) \tag{41}$$

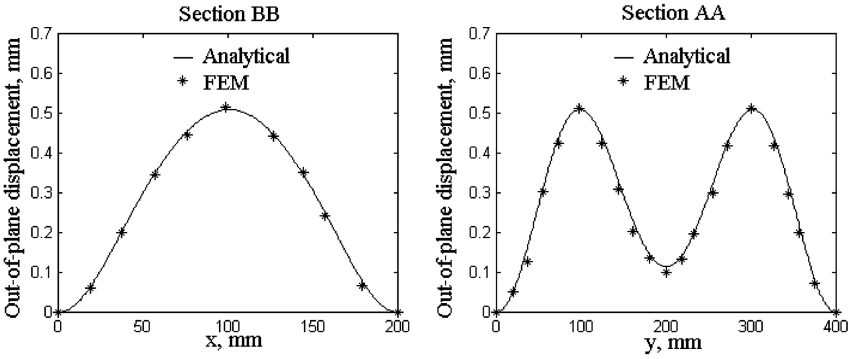

Fig. 21 Out-of-plane displacements for the simply supported light configuration.

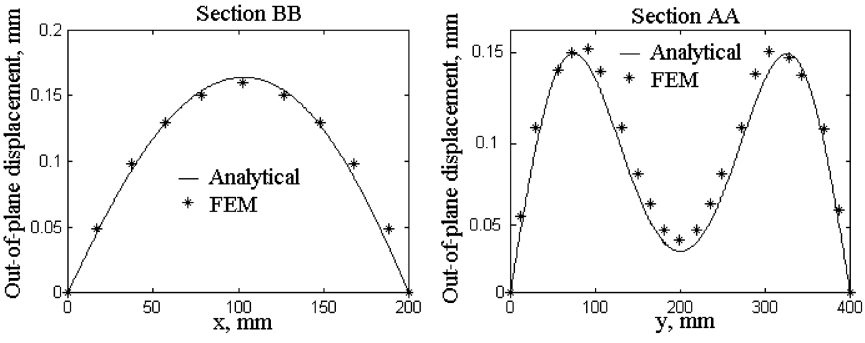

Fig. 22 Out-of-plane displacements for the simply supported medium configuration.

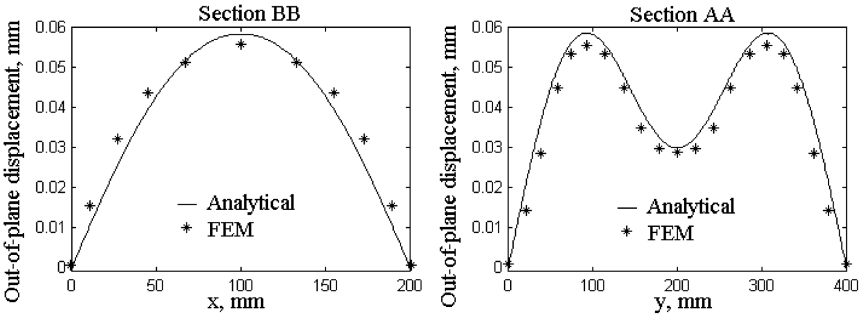

Fig. 23 Out-of-plane displacements for the simply supported heavy configuration.

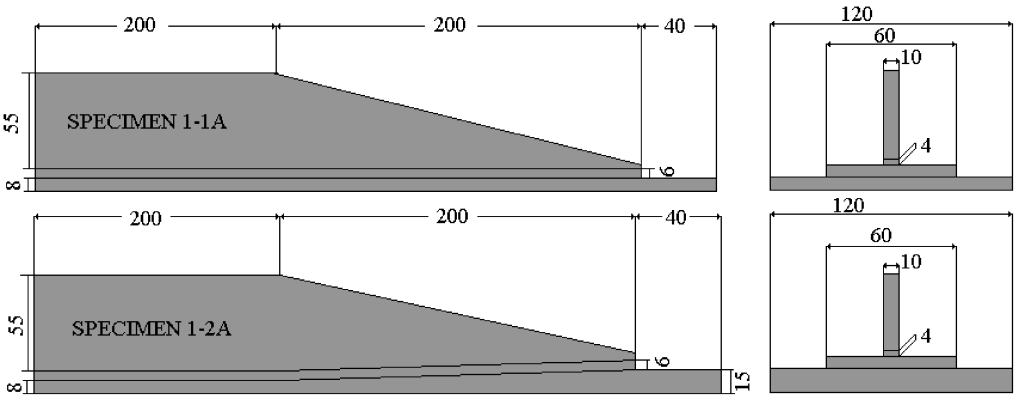

Fig. 24 Schematization of specimens 1-1A and 1-2A, mm.

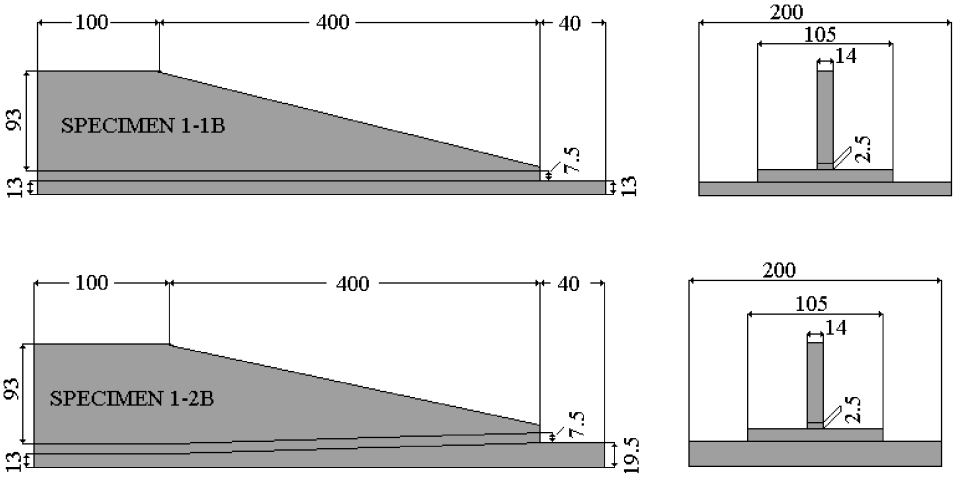

Fig. 25 Schematization of specimens 1-1B and 1-2B, mm.

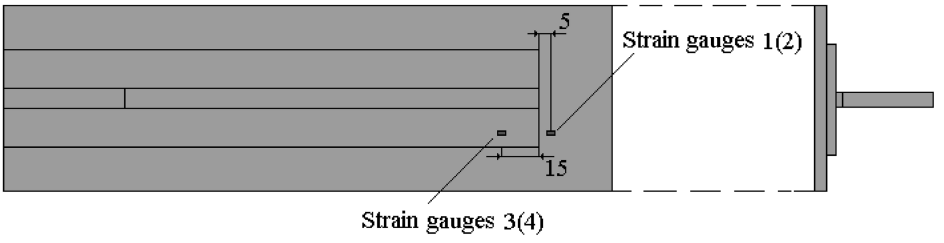

Fig. 26 Strain gauge locations, mm.

It should be emphasized that this solution implies that the deformed shape will be symmetric with respect to the x–z plane (Fig. 27). However, the analyzed configurations behave in such a way that a one-dimensional form might be sufficiently accurate to thoroughly assess its failure; therefore, the error committed neglecting the asymmetry is negligible.

Strain gauge results and predicted responses are compared in Figs. 28–31. Figure 32 summarizes the actual and predicted failure loads. Equation (19) is used to calculate the out-of-plane displacements. Equations (1) and (2) are used to derive normal strains and curvatures. Equations (3) are used to derive the bending moments $\boldsymbol{M}$ and the in-plane normal stress resultants $\boldsymbol{N}$. The

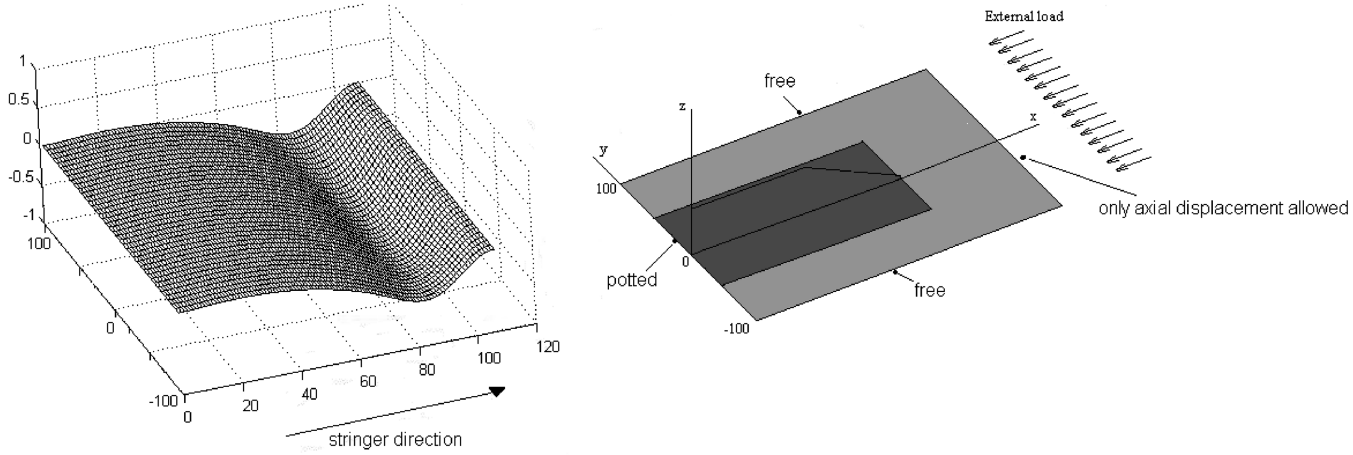

Fig. 27 Predicted out-of-plane displacement of the neutral plane for specimen 1-2B.

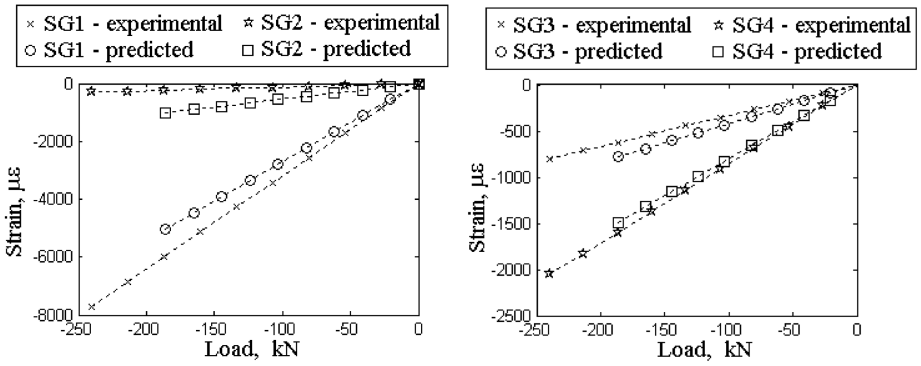

Fig. 28 Strain gauge comparisons for specimen 1-1A.

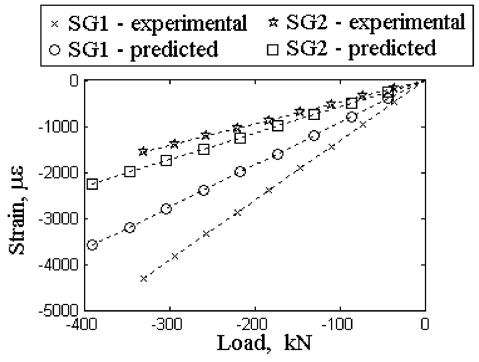

Fig. 29 Strain gauge comparisons for specimen 1-2A.

moments and in-plane resultants are then used to feed Eq. (32) and obtain crack-initiation loads.

Comparisons with strain gauge data further show that the model is slightly stiffer than the tested specimen. This effect is more evident in the proximity of the run-out tip. Although the strain gauge predictions match the test responses quite well for the skin/foot overlap (strain gauge SG3 and SG4, Fig. 24), results for strain gauge SG1 and SG2 are considerably stiffer for all the configurations except for specimen 1-2B. For the latter specimen, the model was able to accurately predict a localized bending of the skin in front of the run-out tip, which is mainly due to the stress concentration in this area. This aspect is interesting because the response is analogous to that of a plate on an elastic foundation in which there are two induced loading components. The first is the vertical component of the resultant load from the stringer that flows into the skin whereas the second is the secondary bending arising from the horizontal component load (tangential to skin) offset from the skin by the

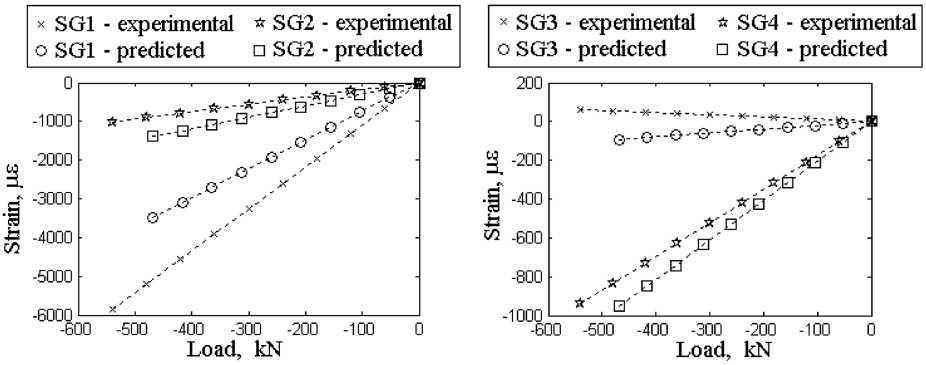

Fig. 30 Strain gauge comparisons for specimen 1-1B.

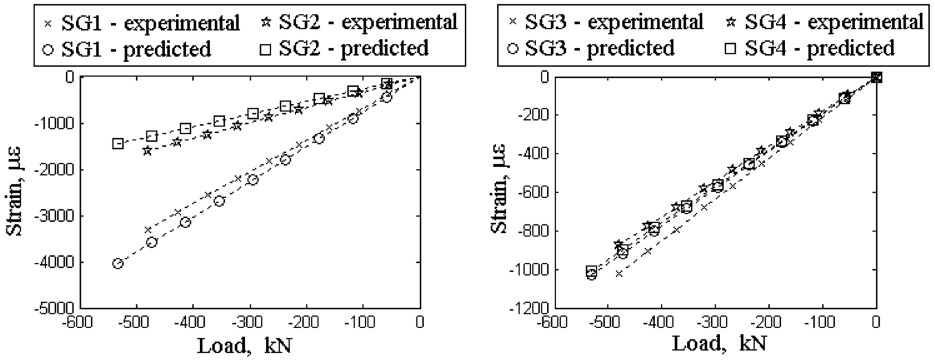

Fig. 31 Strain gauge comparisons for specimen 1-2B.

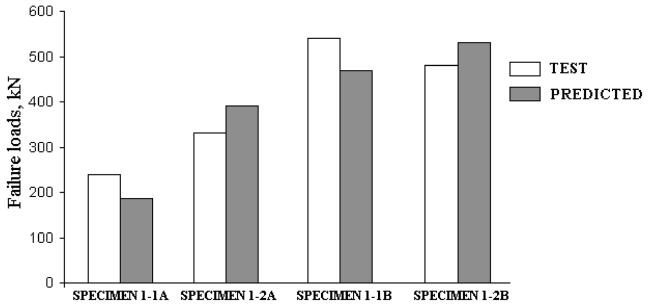

Fig. 32 Predicted and test failure loads.

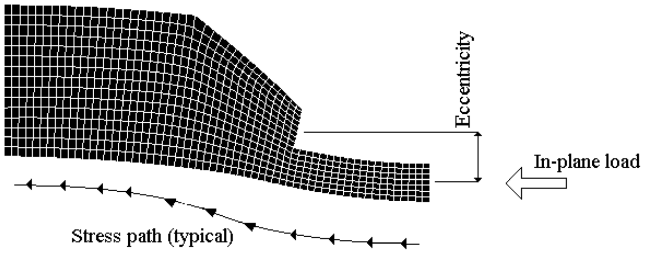

Fig. 33 Typical load path and local eccentricity at the run-out tip (deformed geometry).

eccentricity (see Fig. 33). It is noted that this localized bending is at first linear in character and significantly affects the contributions of modes I and II. Having said this, it is further noted that the nonlinearity inherent in the stress model significantly affects crack-initiation levels. Finally, the failure load predictions match the experimental results quite closely and show that the present analysis is suitable for a preliminary assessment of bonded assemblies.

VI. Discussion

The validation studies undertaken show that the model is suitable to cover an extensive range of configurations and load cases. There is evidence of an intrinsic (local) stiffness of the model for thick designs, suggesting that further assessment is required before using the method for general sizing purposes. Furthermore, the LEFM approach [3] chosen is quite simplistic yet is dominant in the failure load predictions.

In general, the proposed approximate analysis method gives results that are in some cases in excellent agreement with both the FE analysis and the test results. This agreement encourages further studies as the potential of the analysis is only partially expressed in the present paper.

The method is particularly efficient for the analysis of symmetric configurations. Stringers with nonsymmetrical cross sections are subjected to local twist, which cannot be captured by the proposed technique to locally condense the stiffener's properties to a localized additional layer on the skin (see Appendix A).

It must be emphasized that buckling due to in-plane loads is not considered within the present study. Although the model is readily adaptable [17] to predict buckling loads, it cannot be used for postbuckling calculations. Hence, failure modes related to postbuckling are not covered by the analysis. It is also noted that a buckling analysis should also be used in combination with the present method to verify that the predicted failure loads are below critical loads.

However, the current lack of semi-analytical solutions to quickly predict delaminations of composite assemblies increases the utility of the proposed approach to be employed for the preliminary sizing of composite structures. The method is particularly useful if used to model multibay panels. The majority of the methods used by the aerospace industry for the sizing of composite panels are based on simple (analytical or numerical) approaches. Panels are often modeled as skins with a constant thickness, and the influence of the surrounding structure is modeled by enforcing conservative boundary conditions. The present approach allows the simulation of large panels with several stringers and different skin thicknesses in a reasonably fast way, potentially reducing the level of conservatism and improving the global weight saving.

VII. Conclusions

A novel approach based on a combination of the Rayleigh–Ritz method and the Galerkin technique was validated against advanced FE analysis and test results. The Galerkin technique revealed itself to be useful to express the eccentricity of the neutral plane as a superposition of the same eigenfunctions used to employ the Rayleigh–Ritz method. This allows treatment of the eccentricity as an initial moderately small perturbation and expressing it by means of the same basis functions, thus simplifying the final compact form. Currently, the proposed model provides a significantly more efficient analysis of the fracture of stiffened anisotropic panels than those others commonly used. If used for industrial purposes, its accuracy must and can be improved by tuning the exponents of Eq. (32) to fit with the test results and also by defining knockdown factors to render the predictions conservative for all of the comparisons. The approach typically works well for stiffened panels with symmetric stiffeners for which there is an abrupt run out. For these cases, the present approach allows the simulation of large panels with several stringers and different skin thicknesses in a reasonably fast way, potentially reducing the level of conservatism and improving the global weight saving.

Future work is planned to further improve the present analysis by allowing for continuous taper, exploiting the use of nondimensional parameters in parametric optimization studies, and analyzing postbuckling behavior.

Appendix A: Section Properties Condensation

Consider the case reported in Fig. A1. A composite "I" beam is used as a stiffener on a composite skin. As explained before and sketched in Fig. 4, the width of the panel field will equal the foot width. We need to assign an equivalent thickness and an equivalent

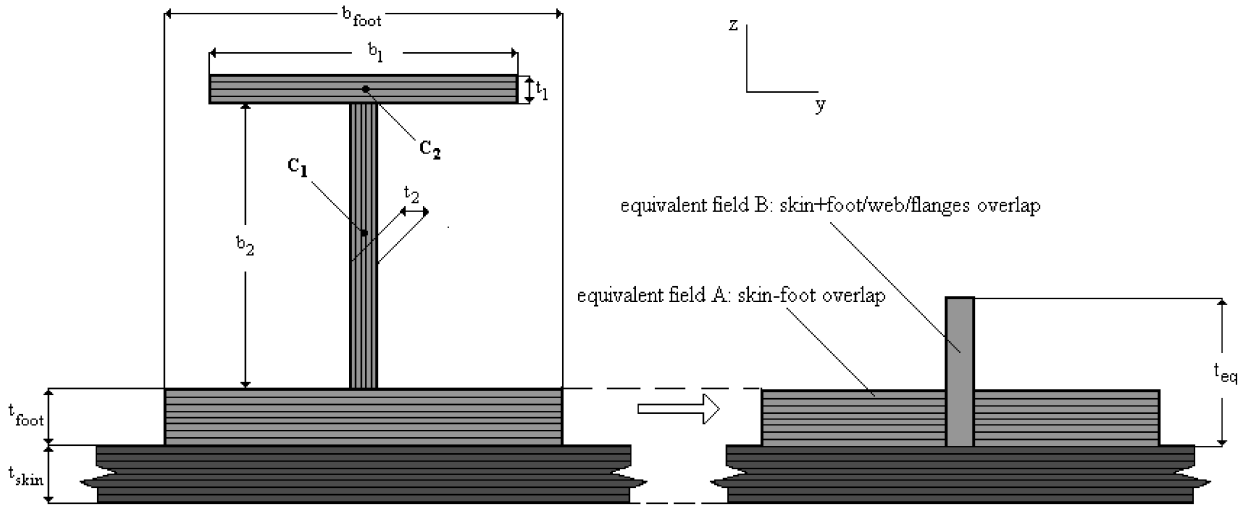

Fig. A1 Condensation of the stringer's properties.

local lamina stiffness matrix $\boldsymbol{Q}^{\text{eq}}$ to the equivalent layer that represents the stiffener. Therefore, we need to properly assess five different quantities:

1) t_{eq}, the equivalent thickness
2) E_x^{eq}, the equivalent stiffness in the x direction
3) E_y^{eq}, the equivalent stiffness in the y direction
4) G_{xy}^{eq}, the equivalent stiffness in the y direction
5) ν_{xy}^{eq}, the equivalent Poisson's ratio

If x is the direction of the main stiffener dimension, E_x^{eq} and t_{eq} are calculated by deriving the global axial (EA_{tot}) and bending (EI_{tot}) of the T beam (the web and upper flange only if referring to Fig. A1) and then imposing the conditions

$$EA_{\text{tot}} = E_x^{\text{eq}} b_{\text{foot}} t_{\text{eq}}, \qquad EI_{\text{tot}} = E_x^{\text{eq}} \tfrac{1}{12} b_{\text{foot}} t_{\text{eq}_{\text{eq}}}^3 \tag{A1}$$

The equivalent elastic modulus in the y direction, that is, orthogonal to the direction of the main stiffener dimension, can be set equal to zero. In fact, it is straightforward to demonstrate that, apart from the lower flange, the remaining part of the stringer will not contribute if the in-plane y loads or the transverse y bending moments are applied.

$$E_y^{\text{eq}} \cong 0 \tag{A2}$$

The equivalent shear modulus is calculated as

$$G_{xy}^{\text{eq}} = \frac{1}{b_{\text{foot}} t_{\text{eq}}} \sum_{k=1}^{n_{\text{flanges}}} G_{xy,k} A_k \tag{A3}$$

where n_{flanges} is the total number of flanges, $G_{xy,k}$ is the shear modulus of the kth flange, and A_k is the area of kth flange

Note that Eq. (A3) neglects the contribution of the vertical webs. Therefore, the formula is particularly valid if thin walled beams are used as stiffeners. All of the contribution should be used if the thicknesses are comparable to the widths. The Poisson's ratios are derived from the assumption that the portion of the stiffener that lies on top of the skin but not directly in contact with it (the web and upper flange if referring to Fig. A1) does not affect the structure's Poisson's ratio when axial loads in the x direction are applied. Hence, the Poisson's ratio ν_{xy}^{eq} equals the Poisson's ratio of the lower flange.

Appendix B: Internal In-Plane Loads Derivation

Decoupling the in-plane load from the transverse displacements and considering that only in-plane loads are acting upon the structure, Eq. (3) reduces to

$$\boldsymbol{\varepsilon}^0 = \boldsymbol{A}^* \boldsymbol{N} \tag{B1}$$

Using this compacted form and enforcing the proper essential and natural boundary conditions, one can obtain the internal in-plane resultants as functions of the external loads applied. The calculation is now expanded for the case described in Figure B1c. Results for the other cases are also summarized. For any other boundary and/or loading conditions, a similar process may be followed.

Equation (B1) can be rewritten in the explicit form as follows:

$$\varepsilon_x^0 = A_{11}^* N_{x,0} + A_{12}^* N_{y,0} + A_{16}^* N_{xy,0} \tag{B2}$$

$$\varepsilon_y^0 = A_{21}^* N_{x,0} + A_{22}^* N_{y,0} + A_{26}^* N_{xy,0} \tag{B3}$$

$$\varepsilon_{xy}^0 = A_{61}^* N_{x,0} + A_{62}^* N_{y,0} + A_{66}^* N_{xy,0} \tag{B4}$$

To guarantee equilibrium at edges i and iii (see Fig. B1c) the condition that the external in-plane x resultant equals the internal in-plane x resultant must hold. If it is further assumed that the in-plane resultants are constant throughout the domain, it follows that

$$N_{x,0} = N_x \tag{B5}$$

Substituting Eq. (B5) into Eqs. (B3) and (B4) and solving with respect to $N_{y,0}$ and $N_{xy,0}$ yields

$$N_{y,0} = -\frac{A_{21}^* A_{66}^* (A_{22}^* - A_{26}^*) + A_{26}^* (A_{62}^* A_{21}^* - A_{61}^* A_{22}^*)}{A_{22}^* A_{66}^* (A_{22}^* - A_{26}^*)} N_x \tag{B6}$$

$$N_{xy,0} = \frac{A_{62}^* A_{21}^* - A_{61}^* A_{22}^*}{A_{66}^* (A_{22}^* - A_{26}^*)} N_x \tag{B7}$$

Equation (B2) is used if the global structure compliance with respect to the external load resultant N_x is sought. Similarly, results for all other configurations sketched in Fig. B1 were calculated and are reported as follows.

Configuration B.1.a:

$$N_{x,0} = N_x, \qquad N_{y,0} = N_{xy,0} = 0 \tag{B8}$$

Configuration B.1.b:

$$N_{x,0} = N_{xy,0} = 0, \qquad N_{y,0} = N_y \tag{B9}$$

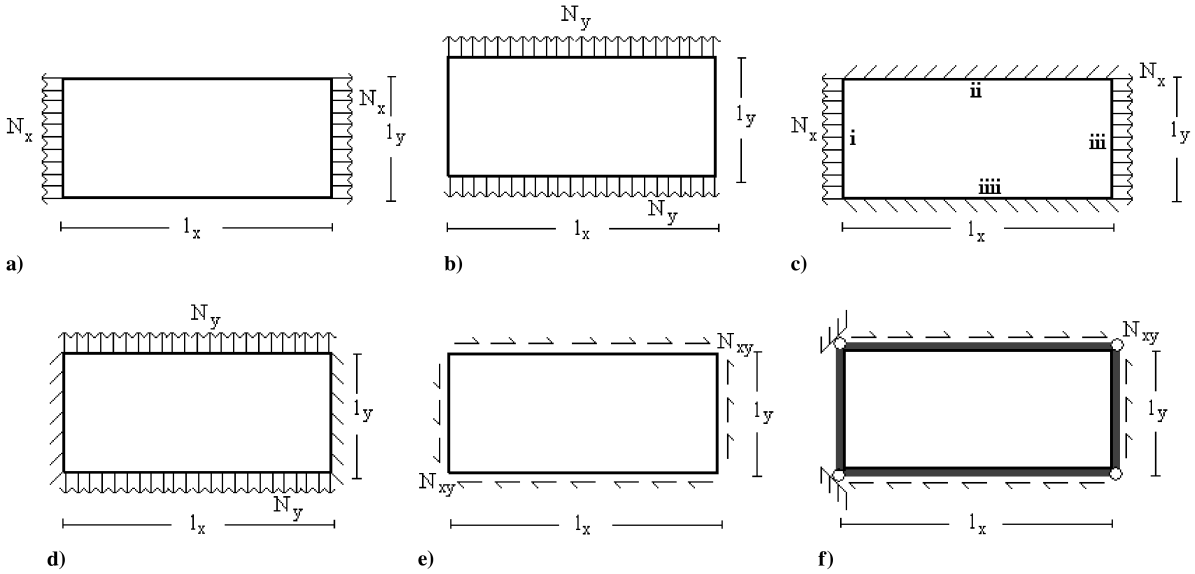

Fig. B1 Examples of possible boundary conditions and external in-plane load applied.

Configuration B.1.d:

$$N_{x,0} = -\frac{A_{12}^*(A_{66}^*A_{11}^* - A_{61}^*A_{16}^*) + A_{16}^*(A_{61}^*A_{12}^* - A_{62}^*A_{11}^*)}{A_{11}^*(A_{66}^*A_{11}^* - A_{61}^*A_{16}^*)}N_y$$

$$N_{y,0} = N_y, \qquad N_{xy,0} = \frac{A_{61}^*A_{12}^* - A_{62}^*A_{11}^*}{A_{66}^*A_{11}^* - A_{61}^*A_{16}^*}N_y \tag{B10}$$

Configuration B.1.e:

$$N_{x,0} = 0, \qquad N_{y,0} = 0, \qquad N_{xy,0} = N_{xy} \tag{B11}$$

Configuration B.1.f:

$$N_{x,0} = -\frac{A_{16}^*(A_{22}^*A_{11}^* - A_{21}^*A_{12}^*) + A_{12}^*(A_{16}A_{21}^* - A_{26}^*A_{11}^*)}{A_{11}^*(A_2^*A_{11}^* - A_{21}^*A_{21}^*)}N_{xy}$$

$$N_{y,0} = \frac{A_{16}^*A_{21}^* - A_{26}^*A_{11}^*}{A_{22}^*A_{11}^* - A_{12}^*A_{21}^*}N_{xy}, \qquad N_{xy,0} = N_{xy} \tag{B12}$$

Appendix C: Eccentricity Discretization

Let $e(x, y)$ be the two-dimensional function describing the neutral plane of the panel. This term is now expressed as a linear combination of coefficients multiplying the problem eigenfunctions plus a certain error component $\mathrm{err}(x, y)$, which represents the fact that the eigenfunctions satisfy the natural and essential boundary conditions of the structural problem, whereas the neutral-plane function does not have to respect this constraint:

$$e = \sum_{i=1}^{\infty} e_i\phi_i(x, y) + \mathrm{err}(x, y) \tag{C1}$$

The Galerkin method consists of arresting the summation at the first $M \times N$ eigenfunctions and enforcing the condition that the components of the error upon the same eigenfunctions equal zero. Recalling that in a Hilbert's space the inner product between two functions is defined as the integral over the domain of the product of the functions, it follows that

$$\int_{x=0}^{l_x}\int_{y=0}^{l_y} \mathrm{err}(x, y)\phi_j(x, y)\,\mathrm{d}x\mathrm{d}y = 0, \quad \forall\ j = 1, \ldots, M \times N \tag{C2}$$

Substituting Eq. (C2) into Eq. (C1) and developing the expressions, a linear system of $M \times N$ equations is obtained. The compact form that allows calculating the unknown $M \times N$ coefficients e_i is

$$\boldsymbol{E} = \boldsymbol{K}^{-1}\boldsymbol{e} \tag{C3}$$

where $\boldsymbol{E}$ is defined by Eq. (21), whereas the vectors $\boldsymbol{e}$ and the matrix $\boldsymbol{K}$ are defined as follows:

$$[\boldsymbol{e}]_j = \int_{x=0}^{l_x}\int_{y=0}^{l_y} e(x, y)\phi_j(x, y)\,\mathrm{d}x\mathrm{d}y \tag{C4}$$

$$[\boldsymbol{K}]_{ij} = \int_{x=0}^{l_x}\int_{y=0}^{l_y} \phi_i(x, y)\phi_j(x, y)\,\mathrm{d}x\mathrm{d}y \tag{C5}$$

Acknowledgments

The first author would like to thank Matthew Beard (Airbus UK, Ltd.) for the financial support provided. Furthermore, the first author would like to express gratitude to Martin Gaitonde and Matt Jevons (Airbus UK, Ltd.) for their constant and precious support. Both authors thank Michael Wisnom for valuable comments.

References

[1] Taki, T., and Kitagawa, T., "Post-Buckling Strength of Composite Stiffened Panel Under Shear Load," AIAA Paper 95-393, 1995.

[2] Falzon, B. J., and Davies, G. A. O., "The Behavior of Compressively Loaded Stiffener Runout Specimens—Part 2: Finite Element Analysis," *Journal of Composite Materials*, Vol. 37, No. 6, 2003, pp. 481–501. doi:10.1177/0021998303037006416

[3] Williams, J. G., "On the Calculation of Energy Release Rates for Cracked Laminates," *International Journal of Fracture*, Vol. 36, No. 2, 1988, pp. 101–119. doi:10.1007/BF00017790

[4] Stevens, K. A., Ricci, R., and Davies, G. A., "Buckling and Post-Buckling of Composite Structures," *Composites*, Vol. 26, No. 3, 1995, pp. 189–199. doi:10.1016/0010-4361(95)91382-F

[5] Dahlen, C., and Springer, G. S., "Delamination Growth in Composites Under Cyclic Loads," *Journal of Composite Materials*, Vol. 28, No. 8, 1994, pp. 738–780.

[6] Falzon, B. J., and Davies, G. A. O., "The Behavior of Compressively Loaded Stiffener Runout Specimens—Part 1: Experiments," *Journal of Composite Materials*, Vol. 37, No. 5, 2003, pp. 381–400. doi:10.1177/0021998303037005407

[7] Hachenberg, D., and Kossira, H., "Theoretical and Experimental Investigation of Stringer Peeling Effects at Stiffened Shear-Loaded

Composite Panels in the Post-Buckling Range," International Council of the Aeronautical Sciences Paper 90-4.3.1, 1990, pp. 511–521.
[8] Corradi-Dell'Acqua, L., *Meccanica delle Strutture. Le Teorie Strutturali ed il Metodo degli Elementi Finiti*, McGraw–Hill, Milan, 1992, pp. 201–206.
[9] Rybiki, E. F., and Kanninen, M. F., "A Finite Element Calculation of Stress Intensity Factors by a Modified Crack Closure Integral," *Engineering Fracture Mechanics*, Vol. 9, No. 4, 1977, pp. 931–938. doi:10.1016/0013-7944(77)90013-3
[10] ABAQUS, Ver. 6.5.1, User Manual, Vol. 4, ABAQUS, Ltd.2004.
[11] Timoshenko, S. P., and Gere, J., *Theory of Elastic Stability*, 2nd ed., McGraw–Hill, New York, 1961, pp. 55, 349.
[12] Timoshenko, S. P., *Theory of Plates and Shells*, McGraw-–Hill, New York, 1940, p. 326.
[13] Wu, F. W., "Application of Fracture Mechanics to Anisotropic Plates," *Journal of Applied Mechanics*, Vol. 34, 1967, pp. 967–974.
[14] Diaconu, C., and Weaver, P., "Approximate Solution and Optimum Design of Compression-Loaded, Postbuckled Laminated Composite Plates," *AIAA Journal*, Vol. 43, No. 4, April 2005, pp. 906–914.
[15] Jones, R. M., *Mechanics of Composite Materials*, Scripta, Washington, D.C., 1975.
[16] Reddy, J. N., *Mechanics of Laminated Composite Plates and Shells*, CRC Press, Boca Raton, FL, 2004.
[17] Kollar, L. P., and Springer, G. S., *Mechanics of Composite Structures*, Cambridge Univ. Press, Cambridge, England, U.K., 2003, Chap. 4.
[18] Dubey, Y. R., *An Approximate Solution to Buckling of Plates by the Galerkin Method*, Pro Quest Company, Ann Arbor, MI, July 2005.
[19] Argawal, B. L., "Postbuckling Behavior of Composite Shear Webs," *AIAA Journal*, Vol. 19, No. 7, July 1981, pp. 933–939.
[20] Davis, D. D. Jr., Farley, G. L., Ambur, D. R., Davis, R. C., Shuart, M. J., Wang, J. T., and Lotts, C. G., "An Analytically Designed Subcomponent Test to Reproduce the Failure of a Composite Wing Box Beam," AIAA Paper 93-1344, 1993.
[21] Timoshenko, S. P., and Gere, J. M., *Theory of Elastic Stability*, 2nd ed., McGraw–Hill, New York, 1961.

F. Pai
Associate Editor